An Early Warning Sign of Critical Transition in The Antarctic Ice Sheet - A New Data Driven Tool for Spatiotemporal Tipping Point

Abd AlRahman AlMomani[1,2] and Erik Bollt[1,2]

[1]Department of Electrical and Computer Engineering, Clarkson University, Potsdam, NY 13699, USA
[2]Clarkson Center for Complex Systems Science (C^3S^2), Potsdam, NY 13699, USA

Abstract

This paper introduces a new tool for data-driven discovery of early warning signs of critical transitions in ice shelves, from remote sensing data. Our approach adopts a directed spectral clustering methodology considering an asymmetric affinity matrix and the associated directed graph Laplacian. We generally applied our approach to reprocessing the ice velocity data and remote sensing satellite images of the Larsen C ice shelf. Our results allow us to (post-cast) predict fault lines responsible for the critical transitions leading to the break up of the Larsen C ice shelf crack, which resulted in the A68 iceberg. We can do so months earlier before the actual occurrence and much earlier than any other previously available methodology, particularly those based on interferometry.

1   Introduction

Warming associated with global climate change causes global sea level to rise Mengel et al. (2016). Three primary reasons for this are ocean expansion McKay et al. (2011), ice sheets lose ice faster than it forms from snowfall, and glaciers at higher altitudes melt. During the 20th century, sea level rise has been dominated by glaciers' retreat. Still, this contribution starts to change in the 21st century because of the increased iceberg calving. Ice sheets store most of the land ice (99.5%) Mengel et al. (2016), with a sea-level equivalent (SLE) of 7.4m for Greenland and 58.3m for Antarctica. Ice sheets form in areas where the snow that falls in winter does not melt entirely over the summer. Over thousands of years of this effect, the layers grow thicker and denser as the weight of new snow and ice layers compresses the older layers.

Ice sheets are always in motion, slowly flowing downhill under their weight. Most of the ice moves through relatively fast-moving outlets called ice streams, glaciers, and ice shelves near the coast. When a marine ice sheet accumulates a mass of snow and ice at the same rate as it loses mass to the sea, it remains stable. Most of Antarctica has yet to see dramatic warming. However, the Antarctic Peninsula, which juts out into relatively warmer waters north of Antarctica, has warmed 2.5 degrees Celsius (4.5 degrees Fahrenheit) since 1950 NASA (2017).

A large area of the Western Antarctic Ice Sheet is also losing mass, probably due to warmer water up-welling from the deeper ocean near the Antarctic coast. In Eastern Antarctica, no clear trend has emerged, although some stations report slight cooling. Overall, scientists believe that Antarctica is starting to lose ice NASA (2017), but so far, the process is not considered relatively fast as compared to the widespread changes in Greenland NASA (2017).

Since 1957, the continent-wide average's current record reveals a surface temperature trend of Antarctica that has been positive and significant at > 0.05 ° C/decade Steig et al. (2009); Gagne et al. (2015). Western Antarctica has warmed by more than 0.1 °C/decade in the last 50 years, and this warming is most active

Figure 1: A-68 iceberg. The fractured berg and shelf are visible in these images, acquired on July 21, 2017, by the Thermal Infrared Sensor (TIRS) on the Landsat 8 satellite. Credit: NASA Earth Observatory images by Jesse Allen, using Landsat data from the U.S. Geological Survey.

during the winter and spring. Although this is partly offset by autumn cooling in Eastern Antarctica, this effect is prevalent in the 1980s and 1990s Steig et al. (2009).

Of particular interest to us in this presentation, the Larsen Ice Shelf extends like a ribbon of the ice shelf, down from the East Coast of the Antarctic Peninsula, from James Ross Island to the Ronne Ice Shelf. It consists of several distinct ice shelves, separated by headlands. The major Larsen C ice crack was already noted to have started in 2010 Jansen et al. (2015). Still, it was initially very slowly evolving, and there were no signs of radical changes according to Interferometry processing of the remote sensing imagery Jansen et al. (2010b). However, since October 2015, the major ice crack of Larsen C has been growing faster, until the point more recently, it finally failed, resulting in calving the massive A68 iceberg. See Fig. 1; this is the largest known iceberg, with an area of more than 2,000 square miles, or nearly the size of Delaware. In summary, A68 detached from one of the largest floating ice shelves in Antarctica and floated off in the Weddell Sea.

In Glasser et al. (2009), the authors presented a structural glaciological description of the system and subsequent analysis of surface morphological features of the Larsen C ice shelf, as seen from satellite images spanning the period 1963–2007. The research results and conclusions stated that: "*Surface velocity data integrated from the grounding line to the calving front along a central flow line of the ice shelf indicate that the residence time of ice (ignoring basal melt and surface accumulation) is 560 years. Based on the distribution of ice-shelf structures and their change over time, we infer that the ice shelf is likely to be a relatively stable feature and that it has existed in its present configuration for at least this length of time.*".

In Jansen et al. (2010a), the authors modeled the flow of the Larsen C and northernmost Larsen D ice shelves using a model of continuum mechanics of the ice flow. They applied a fracture criterion to the simulated velocities to investigate the ice shelf's stability. The conclusion of that analysis shows that the Larsen C ice shelf is inferred to be stable in its current dynamic regime. This work was published in 2010. According to analytic studies, the Larsen C ice crack already existed in the same year, but at its slow-growing rate. There were no expectations at that time for the fast-growing and collapse that happened for Larsen C.

Interferometry has traditionally been the primary technique to analyze and predict ice cracks based on remote sensing. Interferometry Bassan (2014); Lämmerzahl et al. (2001), is based on a family of techniques in which waves, usually electromagnetic waves, are superimposed, causing the phenomenon of interference
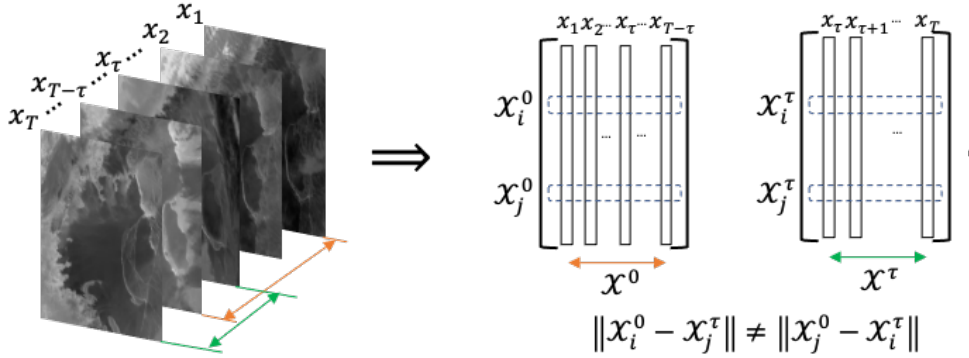
Figure 2: Directed partitioning method. We see the image sequence to the left, and to the right, we reshape each image as a single column vector. Following the resultant trajectories, we see that the pairwise distance between the two matrices will result in an asymmetric matrix. Raw images source Scambos et al. (1996).

patterns, which in turn are used to extract information concerning the underlying viewed materials. Interferometers are widely used across science and industry to measure small displacements, refractive index changes, and surface irregularities. So it is considered a robust and familiar tool that is successful in the macro-scale application of monitoring the structural health of the ice shelves. So it is our job here to contrast our methodology to interferometry. Here we will take a data-driven approach directly from the remote sensing imagery to infer structural changes of the impending tipping point to Larsen C's break's critical transition.

Fig. A.1 shows the interferometry image as of April 20, 2017, and although it clearly shows the crack that already existed, but may provide no information or forecasting powers indicating what can happen next. Just a couple of weeks after the image shown in Fig. A.1, the Larsen C ice crack changed significantly and took a different dynamic that quickly after that divided into two branches, as shown in Fig. A.2. As we will show, our method will achieve a much more successful and early data-driven indicator of this important outcome.

2   Directed Partitioning

In our previous work Al Momani (2017); AlMomani and Bollt (2018), we developed the method of Directed Affinity Segmentation (DAS). We showed high performance in successfully detecting coherent structures in fluidic systems, observed from "movie data" and without the need for the intermediate stage of finding the vector field responsible for underlying advection.

Two of the most commonly used and successful image segmentation methods are based on 1) the k-means Kanungo et al. (2002), and 2) spectral segmentation Ng et al. (2002), respectively. However, while these were developed successfully for static images, these methods need major adjustments for successful application to sequences of images. The spatiotemporal problem of motion segmentation is associated with coherence, despite that traditionally, they are considered well suited to static images Shi and Malik (2000). The key difference is what underlies a notion of coherent observations that we must also understand directionality associated with the arrow of time.

Affinity measure is the phrasing for comparison, or cost, between states, and as such, a loss function of some kind of often the starting point for many algorithms in machine learning. However, when there is an underlying arrow of time, the loss functions that most naturally arise when tracking coherence are inherently not symmetric. Correspondingly, affinity matrices associate the affinity measure for each pairwise comparison across a finite data set. It is also useful to consider the undirected graph associated with the affinity matrix, where there is an edge between each state for which there is a nonzero affinity. Generally, in the symmetric

case, these graphs are undirected. Now consider that if the affinity matrices are not symmetric, then these are associated with *directed graphs.* This is a theoretical complication to standard methodology since much of the theoretical underpinnings of standard spectral partitioning assumes a symmetric matrix corresponding to an undirected graph and then considers the spectrum of its corresponding symmetric Laplacian matrix that follows. This can be accommodated by methods considering the spectral theory of graph Laplacian for weighted directed graphs, built upon the theoretical work of F. Chung Chung and Oden (2000), and as we built upon in AlMomani and Bollt (2018).

Before proceeding with our directed partitioning method, we formulate the (movie) imagry data set as the following matrices;

$$\mathcal{X}^0 = [X_1|X_2|...|X_{T-\tau}], \tag{1}$$

$$\mathcal{X}^\tau = [X_{\tau+1}|X_{\tau+2}|...|X_T], \tag{2}$$

where each X_i is the ith image (or the image at i^{th} time step) reformed as a column vector, See Fig. 2, τ is the time delay, $\mathcal{X}_0$ and $\mathcal{X}_\tau$ are the images sequences stacked as column vectors with a time delay at the current and future times respectively. Choosing the value of the time delay τ, can results in significant differences in the segmentation process. Consider that in the case of a relatively slowly evolving dynamical system, where the change between two consecutive images is not significantly distinguishable, then choosing a large value for τ may be better suited. In our work, we considered the mean image over a period of one-month as a moving window generates our images, which implies τ to be one month.

Note that the rows of $\mathcal{X}^0, \mathcal{X}^\tau \in \mathbb{R}^{d \times T-\tau}$ represent the change of the color of the pixel at a fixed spatial location z_i. It is crucial to keep in mind that we chose the color as the evolving quantity for a designated spatial location for clarity and consistency with our primary application and approach introduced in this paper. However, we can select the evolving quantity to be the magnitude of the pixels obtained from spectral imaging or experimental measures obtained from the field, such as pressure, density, or velocity. The results section introduces examples where we used the ice surface velocity instead of the color to show how results may vary based on the selected measure.

We introduced AlMomani and Bollt (2018) an affinity matrix in terms of a pairwise distance function between the pixels i and j as,

$$D_{i,j} = \mathcal{S}(\mathcal{X}_i^0, \mathcal{X}_j^\tau) + \alpha \mathcal{C}(\mathcal{X}_i^0, \mathcal{X}_j^\tau, \tau) \tag{3}$$

where $\mathcal{S} : \mathbb{R}^2 \mapsto \mathbb{R}$ is the spatial distance between z_i and z_j, and $\mathcal{C} : \mathbb{R}^{T-\tau} \times \mathbb{R}^{T-\tau} \times \mathbb{R} \mapsto \mathbb{R}$ is a distance function describing "color distance" the ith and the jth color channels. The parameter $\alpha \geq 0$ regularizes balancing these two effects. The value of α can be seen as a degree of importance of the function $\mathcal{C}$ to the spatial change. Large values of α will make the change color, for example, dominate the distance in Eq. 3. It will then classify "very" close (spatially) regions as different coherent sets when they have small color differences. On the other hand, small values of α may classify spatially neighboring regions as one coherent set, even when they have a significant color difference. In our work, we scaled the value of $\mathcal{S}$ and $\mathcal{C}$ to be in $[0, 1]$, then we choose $\alpha = 0.25$, to keep the focus on the spatial change, where we choose the functions $\mathcal{S}$ and $\mathcal{C}$ each to be L_2-distances,

$$\mathcal{S}(\mathcal{X}_i^0, \mathcal{X}_j^\tau) = \|z_i - z_j\|_2, \tag{4}$$

and

$$\mathcal{C}(\mathcal{X}_i^0, \mathcal{X}_j^\tau, \tau) = \|\mathcal{X}_i^0 - \mathcal{X}_j^\tau\|_2. \tag{5}$$

We see that the spatial distance matrix $\mathcal{S}$ is symmetric, however, the color distance matrix $\mathcal{C}$ is asymmetric for all $\tau > 0$. Then, while the matrix generated by $\mathcal{C}(\mathcal{X}_i^0, \mathcal{X}_j^\tau, 0)$ refers to the symmetric case of spectral clustering approaches, we see that the matrix given by $\mathcal{C}(\mathcal{X}_i^0, \mathcal{X}_j^\tau, \tau)$, $\tau > 0$ implies an asymmetric cost naturally due to the directionality of the arrow of time. Thus we require an asymmetric clustering approach should be adopted.

First we define our affinity matrix from Eq. 3 as,

$$\mathcal{W}_{i,j} = e^{-D_{i,j}^2/2\sigma^2}. \tag{6}$$

This has the effect that both spatial and measured (color) effects have "almost" Markov properties, as far field effects are almost "forgotten" in the sense that they are almost zero, and near field values are largest. Notice we have suppressed including all the parameters in writing $\mathcal{W}_{i,j}$, and that besides time parameter τ that serve as sampling and history parameters, together the parameters α and σ serve to balance spatial scale and resolution of color histories.

We proceed to cluster the spatiotemporal regions of the system, in terms of the directed affinity $\mathcal{W}$ by interpreting the problem as random walks through the weighted *directed* graph, $G = (V, E)$ designed by $\mathcal{W}$ as a weighted adjacency matrix. Let,

$$\mathcal{P} = \mathcal{D}^{-1}\mathcal{W}, \tag{7}$$

where

$$\mathcal{D}_{i,j} = \begin{cases} \sum_k \mathcal{W}_{i,k}, i = j, \\ 0, i \neq j, \end{cases} \tag{8}$$

is the degree matrix, and $\mathcal{P}$ is a row stochastic matrix representing probabilities of a Markov chain through the directed graph G. Note that $\mathcal{P}$ is row stochastic implies that it row sums to one. This is equivalently stated that the right eigenvector is the ones vector, $\mathcal{P}\mathbf{1} = \mathbf{1}$, but the left eigenvector corresponding to left eigenvalue 1 represents the steady state row vector of the long term distribution,

$$u = u\mathcal{P}, \tag{9}$$

which for example if $\mathcal{P}$ is irreducible, then $u = (u_1, u_2, ..., u_{pq})$ has all positive entries, $u_j > 0$ for all j, or say for simplicity $u > 0$. Let Π be the corresponding diagonal matrix,

$$\Pi = diag(u), \tag{10}$$

and likewise,

$$\Pi^{\pm 1/2} = diag(u^{\pm 1/2}) = diag((u_1^{\pm 1/2}, u_2^{\pm 1/2}, ..., u_{pq}^{\pm 1/2})), \tag{11}$$

which is well defined for either $\pm$ sign branch when $u > 0$.

Then, we may cluster the directed graph by concepts of spectral graph theory for directed graphs, following the weighted directed graph Laplacian described by Fan Chung Chung (2005), and a similar computation has been used for transfer operators in Froyland and Padberg (2009); Hadjighasem et al. (2016) and as reviewed Bollt and Santitissadeekorn (2013); Santitissadeekorn and Bollt (2007); Bollt et al. (2012), including in oceanographic applications. The Laplacian of the directed graph G is defined, Chung (2005),

$$\mathcal{L} = I - \frac{\Pi^{1/2}\mathcal{P}\Pi^{-1/2} + \Pi^{-1/2}\mathcal{P}^T\Pi^{1/2}}{2}. \tag{12}$$

The first smallest eigenvalue larger than zero, $\lambda_2 > 0$ such that,

$$\mathcal{L}v_2 = \lambda_2 v_2, \tag{13}$$

allows a bi-partition, by,

$$y = \Pi^{-1/2}v_2, \tag{14}$$

by sign structure. Analogously to the Ng-Jordan-Weiss symmetric spectral image partition method Ng et al. (2002), the first k eigenvalues larger than zero, and their eigenvectors, can be used to associate a multi-part partition, by the assistance of k-means clustering these eigenvectors. By defining the matrix $V = [v_1, v_2, \ldots, v_k]$, that have the eigenvectors associated with the kth largest eigenvalues on its columns, then we use the k-means clustering to multi partition V based on the L_2 distance between V's rows. Each row in the matrix V is associated with a specific spatial location (pixel), then by reshaping the labels vector that results from the k-means clustering, we obtain our labeled image.
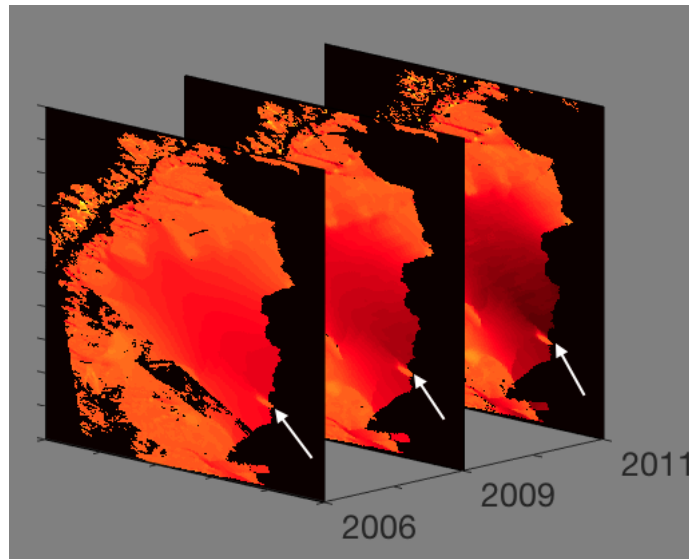
Figure 3: Ice surface velocity. The figure shows the data set for three different years around the beginning of the Larsen C ice crack in 2010. The data from the years 2007,2008 and 2010 have corrupted data on the region of interest, and then they are excluded. The color scale indicates the magnitude of the velocity from light red (low velocity) to dark red (high velocity), and the arrow points to the starting tip of the crack. The result of the directed partitioning is shown in Fig. 4. Source of data: E. Rignot, J. Mouginot and B. Scheuchl (2017).
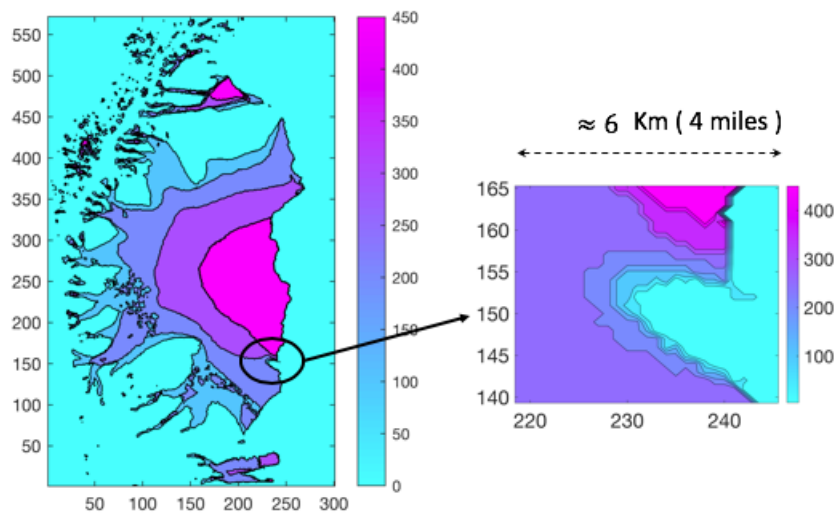
Figure 4: Directed Affinity result. (Left) The directed partitioning results for the ice surface velocity of 2006, 2009, 2011, and 2012. Note that the ice shelf crack started in 2010. (Right) A narrow field zoom to the region of interest shows large variations of ice surface velocity within a small area, to give a clearer focused view of the differences in speeds. In Appendix, Fig. B.1 shows the surface plot for the same result.

3 Results

We apply the directed affinity segmentation to satellite images of Larsen C ice shelf and ice surface velocity data. Here we show that the directed affinity segmentation of spatiotemporal changes can work as an early warning sign tool for critical transition in marine ice sheets. We will apply our "post-casting" experiments on Larsen C images before the splitting of the A68 iceberg. Then we will compare our forecasting based on segmentation results to the actual unfolding of the event.

In Fig. 3, we see different snapshots of the ice surface velocity data set E. Rignot, J. Mouginot and B. Scheuchl (2017); Rignot et al. (2011); Mouginot et al. (2012), which is part of the NASA Earth system data records for use in research environments (MEaSUREs) program. It provides the first comprehensive E. Rignot, J. Mouginot and B. Scheuchl (2017), high-resolution, digital mosaics of ice motion in Antarctica assembled from multiple satellite interferometric synthetic-aperture radar systems. We apply our directed affinity partitioning algorithm to these available data sets, and the results are shown as a labeled image in Fig. 4.

As shown in Fig. 4, we note the following:

- The data collected from eight different sources E. Rignot, J. Mouginot and B. Scheuchl (2017); Map (2017), with different coverage and various error ranges, and interpolating the data from different sources explains the smooth curves in segmentation around the region of interest.

- The directed partitioning shows the Larsen C ice shelf as a nested set of coherent structures that are contained successively within each other.

- The zoom picture highlights shown in the right of Fig. 4 show the region where the Larsen C ice crack starts. Furthermore, we see a significant change of velocity within a narrow spatial distance (4 miles). More precisely, the outer boundaries of coherent sets become spatially very close (considering the margin of error in the measurements Map (2017). We conclude with high probability that these contact).

Directed partitioning gives us informative clustering, meaning that each cluster has homogeneous properties, such as the magnitude and the direction of the velocity. Consider the nested coherent sets, $A_1 \subset A_2 \subset ... \subset A_n$, shown in Fig. 5. Each set A_{i-1} maintains its coherence within A_i because of a set of properties (i.e., chemical or mechanical properties) that rules the interaction between them. However, observe that the contact between the boundaries of the sets A_{i-1} and A_i, can mean a direct interaction between A_{i-1} and A_{i+1}. These later sets may significantly differ in their properties, such as a significant difference of velocity, which may require different analysis under different assumptions than the gradual increase in the velocity.

However, since the sets boundaries are not entirely contacted. The velocities' directions reveal no critical changes; we believe this results implicitly from the data preprocessing nature that includes interpolation and smoothing of the measurements. We believe that the interpolation and smoothing of the measurements cause loss of data informativity about critical transitions. Our method, using the ice surface velocity data, was able to detect more details. However, it still cannot detect critical transitions such as the crack branching, as discussed in the introduction, and shown as in Fig. A.2. Based on our results using the ice velocity data, we state nothing more than such close interaction between coherent sets boundaries, as shown in Fig. 4, can be an early warning sign that should be considered and investigated by applying potential hypothesis ("what if" assumptions) and analyzing the consequences from any change or any error in the measured data.

As a matter of declaring our approach's success over standard methodology, observe that our directed partitioning method achieves better results using the remote sensing satellite images Scambos et al. (1996) as in contrast to the standard and already respected interferometry concept. To reduce the obscuration effects of noise (clouds and image variable intensity), we used the averaged images, over one month, as a single snapshot for the directed affinity constructions. Fig. 6, the directed affinity partitioning for two time-windows starts from December 2015. Notice that the directed partitioning begins to detect the Larsen C ice shelf's significant change in July 2016. In Fig. 7, we see that by September 2016, we detect a structure very close in shape to the eventual and actual iceberg A-68, which calved from Larsen C in July 2017. Moreover,
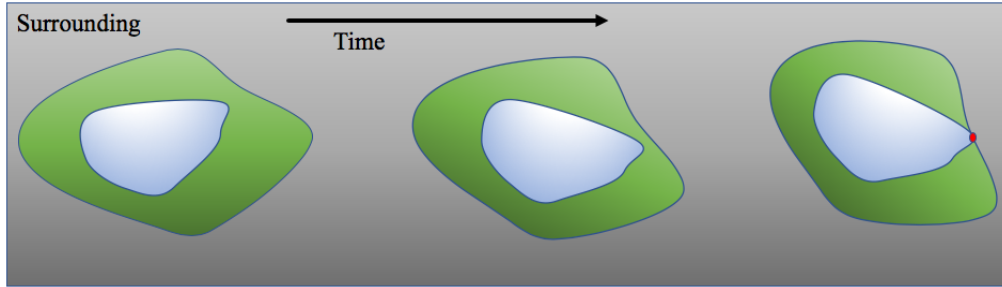
Figure 5: Two coherent sets dynamic. As the inner set contact the boundaries of the outer one, than give the chance for a new reactions that "may" cause critical transition.

by November 2016, see Fig. B.2, the boundaries of the detected partitions match the crack dividing into two branches that happened in later in May 2017 and shown in Fig. A.2.

4 Discussion

We have presented a new approach for predicting possible critical transitions in spatiotemporal systems, specifically marine ice sheets, based on remote sensing satellite imagery. Our approach shows reliability in detecting coherent structures, and when the object of concern is a rigid body such as ice sheets. The main idea is that observing a significant and perhaps topological form change of a coherent structure may indicate an essential underlying critical structural change of the ice over time. The computational approach is based on spectral graph theory in terms of the directed graph Laplacian. In the case of the Larsen C ice shelf, this is born out. We successfully observe the calving of the A68 iceberg months before the primary competing method based on interferometry. This transition of the coherent structure can indicate a possible fracture along the edges of directed affinity partitioning. We see that the directed affinity partitioning can be a useful early warning sign that indicates the possibility of critical spatiotemporal transitions, and it can help to bring the attention to specific regions to investigate different possible scenarios in the analytic study, whether computational or possibly even supporting further field studies and deployed aerial remote sensing missions.

In our future work, we plan to pursue the idea of connecting our data-driven approach of computing boundaries by directed partitioning with the computational science approach in terms of stress/strain analysis of rigid bodies and an understanding of the underlying physics. In addition to expressing the risk of the possible critical transitions of multiple coherent structures that surround each other in terms of Lyapunov exponent analysis of the minimum distance between two evolving shape coherence described by finite time curvatures Ma and Bollt (2014, 2015); Ma et al. (2016) that surround each other.

5 Acknowledgments

This work was funded in part by the Army Research Office, the Naval Research Office, and also DARPA.

References

E. S. Agency. ESR: LARSEN C CRACK INTERFEROGRAM. Contains modified Copernicus Sentinel data (2017), processed by A. Hogg/CPOM/Priestly Centre. https://m.esa.int/spaceimages/Images/2017/04/Larsen-C_crack_interferogram, 2017. Accessed: 2020-04-28.
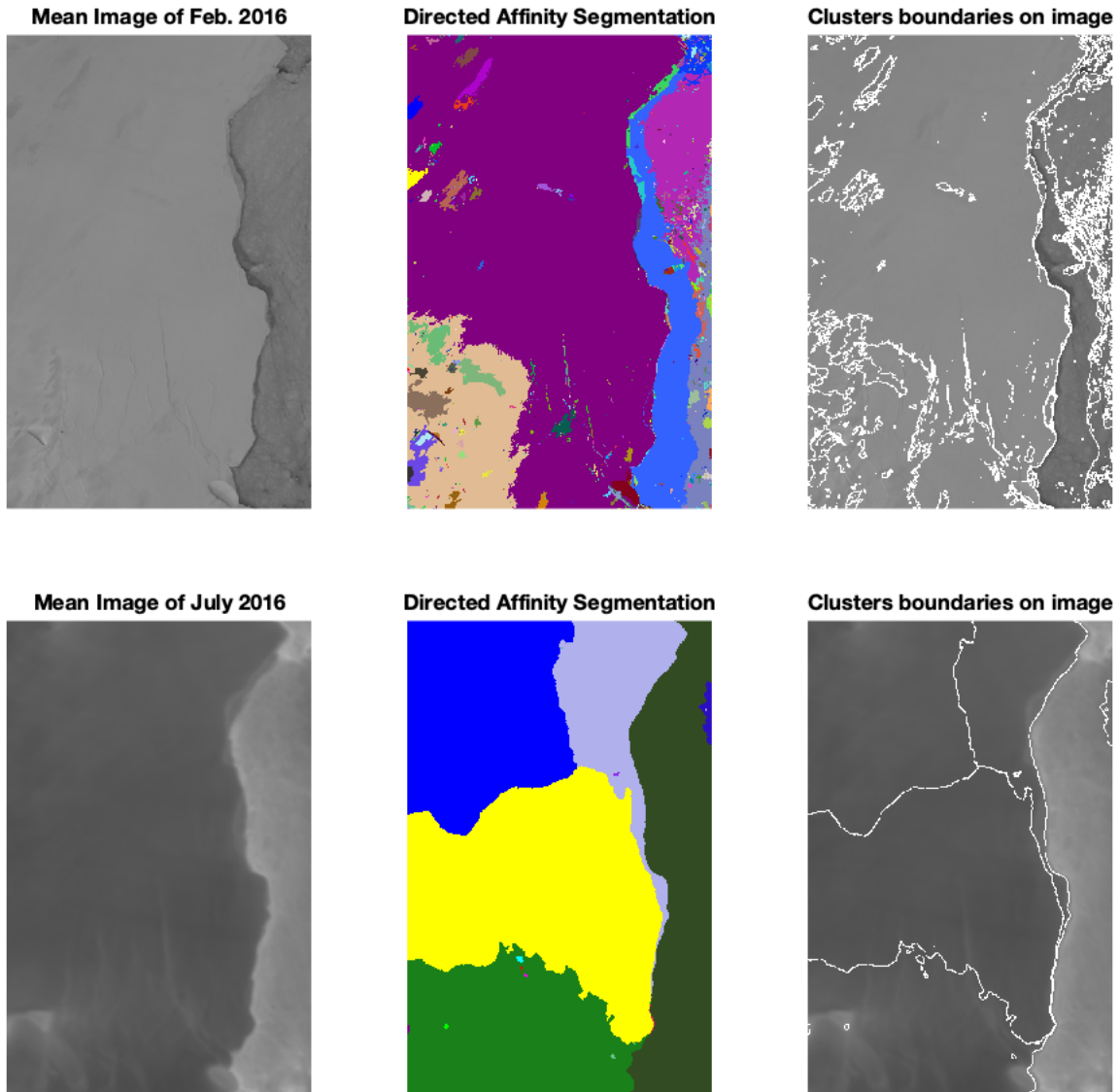
Figure 6: For two time-windows (top and bottom), we see (Left) The mean image of the images included in the window. (Middle) The Directed Affinity Segmentation Labeled Clusters. (Right) Overlying the directed affinity segmentation boundaries over the mean image of the window. We took these time windows of Feb. 2016 and July 2016 as a detailed example, and more time windows results are shown in Fig. 7. We see that during 2016, there was no significant change in Larsen C crack at the beginning of the year. In July 2016, and based solely on data up to that point in time, the directed affinity segmentation propose a large change in the crack dynamics, and this change keeps going faster as Fig. 7 shows. Raw images source Scambos et al. (1996).
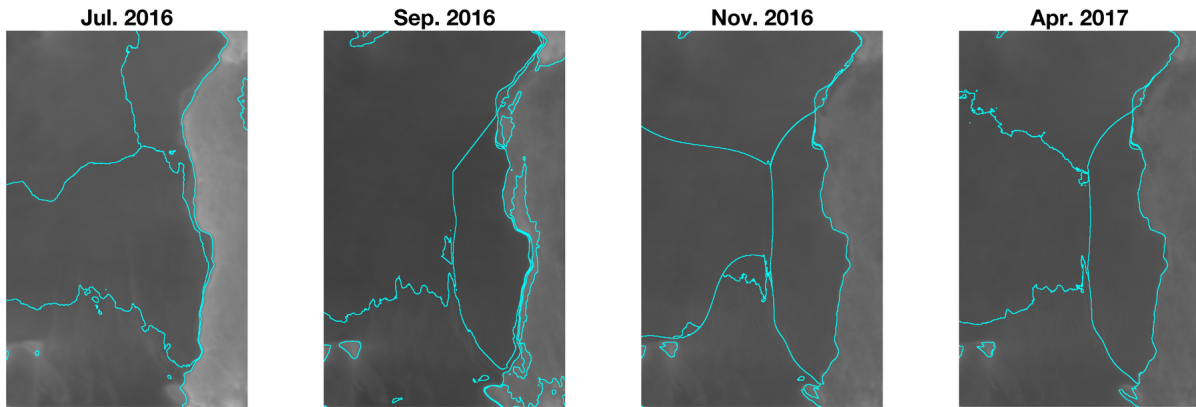
Figure 7: In analogy to Fig. 6-Right, this figure shows the Directed Affinity Segmentation boundaries for different time windows starting from July 2016 to April 2017. Raw images source Scambos et al. (1996).
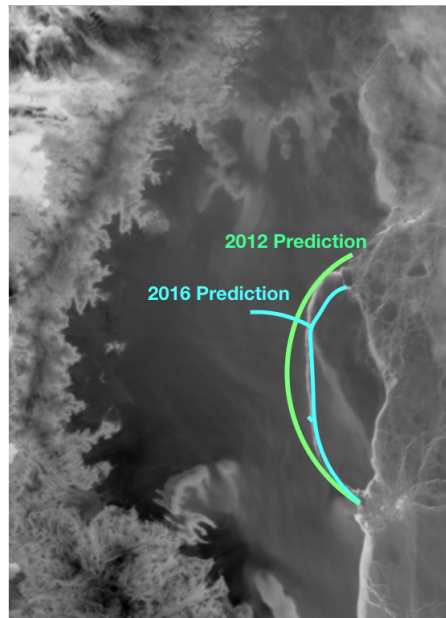
Figure 8: 2012 prediction based on ice surface velocity data, and 2016 prediction based only on satellite images. Compare to the actual crack (white curve between the two prediction curves) on July 2017, shown in Fig. 1. Raw image source Scambos et al. (1996).

A. A. R. R. Al Momani. *Coherence from Video Data Without Trajectories: A Thesis*. PhD thesis, Clarkson University, 2017.

A. AlMomani and E. Bollt. Go With the Flow, on Jupiter and Snow. Coherence from Model-Free Video Data Without Trajectories. *Journal of Nonlinear Science*, 2018. ISSN 14321467. doi: 10.1007/s00332-018-9470-1.

M. Bassan. Advanced interferometers and the search for gravitational waves. *Astrophysics and Space Science Library*, 404:275–290, 2014.

E. Bollt and N. Santitissadeekorn. Applied and computational measurable dynamics. *Society for Industrial and Applied Mathematics*, 2013.

E. M. Bollt, A. Luttman, S. Kramer, and R. Basnayake. Measurable dynamics analysis of transport in the gulf of mexico during the oil spill. *International Journal of Bifurcation and Chaos*, 22(03):1230012, 2012.

F. Chung. Laplacians and the cheeger inequality for directed graphs. *Annals of Combinatorics*, 9:1–19, 2005.

F. Chung and K. Oden. Weighted graph Laplacians and isoperimetric inequalities. *Pacific Journal of Mathematics*, 2000. ISSN 0030-8730. doi: 10.2140/pjm.2000.192.257.

G. Froyland and K. Padberg. Almost-invariant sets and invariant manifolds - Connecting probabilistic and geometric descriptions of coherent structures in flows. *Physica D: Nonlinear Phenomena*, 238(16):1507–1523, 2009. ISSN 01672789. doi: 10.1016/j.physd.2009.03.002.

M. Gagne, N. Gillett, and J. Fyfe. Observed and simulated changes in antarctic sea ice extent over the past 50 years. *Geophysical Research Letters*, 42(1):90–95, 2015.

N. F. Glasser, B. Kulessa, A. Luckman, D. Jansen, E. C. King, P. R. Sammonds, T. A. Scambos, and K. C. Jezek. Surface structure and stability of the Larsen C ice shelf, Antarctic Peninsula. *Journal of Glaciology*, 2009. ISSN 00221430. doi: 10.3189/002214309788816597.

A. Hadjighasem, D. Karrasch, H. Teramoto, and G. Haller. Spectral-clustering approach to Lagrangian vortex detection. *Physical Review E - Statistical, Nonlinear, and Soft Matter Physics*, 93(6), 2016. ISSN 15502376. doi: 10.1103/PhysRevE.93.063107.

D. Jansen, B. Kulessa, P. R. Sammonds, A. Luckman, E. C. King, and N. F. Glasser. Present stability of the Larsen C ice shelf, Antarctic Peninsula. *Journal of Glaciology*, 2010a. ISSN 00221430. doi: 10.3189/002214310793146223.

D. Jansen, B. Kulessa, P. R. Sammonds, A. Luckman, E. C. King, and N. F. Glasser. Present stability of the Larsen C ice shelf, Antarctic Peninsula. *Journal of Glaciology*, 2010b. ISSN 00221430. doi: 10.3189/002214310793146223.

D. Jansen, A. J. Luckman, A. Cook, S. Bevan, B. Kulessa, B. Hubbard, and P. Holland. Brief communication: Newly developing rift in larsen c ice shelf presents significant risk to stability. *Cryosphere*, 9(3):1223–1227, 2015.

T. Kanungo, D. Mount, N. Netanyahu, C. Piatko, R. Silverman, and A. Wu. An efficient k-means clustering algorithm: analysis and implementation. *IEEE Transactions on Pattern Analysis and Machine Intelligence*, 24(7):881–892, 2002. ISSN 0162-8828. doi: 10.1109/TPAMI.2002.1017616.

C. Lämmerzahl, C. F. Everitt, and F. W. Hehl. *Gyros, Clocks, Interferometers...: Testing Relativistic Gravity in Space*, volume 562. Springer Science & Business Media, 2001.

T. Ma and E. M. Bollt. Differential geometry perspective of shape coherence and curvature evolution by finite-time nonhyperbolic splitting. *SIAM Journal on Applied Dynamical Systems*, 13(3):1106–1136, 2014.

T. Ma and E. M. Bollt. Shape coherence and finite-time curvature evolution. *International Journal of Bifurcation and Chaos*, 25(05):1550076, 2015.

T. Ma, N. T. Ouellette, and E. M. Bollt. Stretching and folding in finite time. *Chaos: An Interdisciplinary Journal of Nonlinear Science*, 26(2):023112, 2016.

M. I.-B. A. I. V. Map. MEaSUREs InSAR-Based Antarctica Ice Velocity Map, Version 2. https://nsidc.org/data/nsidc-0484/versions/2{#}data, 2017. Accessed: 2018-09-17.

N. P. McKay, J. T. Overpeck, and B. L. Otto-Bliesner. The role of ocean thermal expansion in last interglacial sea level rise. *Geophysical Research Letters*, 38(14), 2011.

M. Mengel, A. Levermann, K. Frieler, A. Robinson, B. Marzeion, and R. Winkelmann. Future sea level rise constrained by observations and long-term commitment. *Proceedings of the National Academy of Sciences*, 2016. ISSN 0027-8424. doi: 10.1073/pnas.1500515113. URL https://www.pnas.org/content/early/2016/02/17/1500515113.

J. Mouginot, B. Scheuchl, and E. Rignot. Mapping of ice motion in antarctica using synthetic-aperture radar data. *Remote Sensing*, 4(9):2753–2767, 9 2012. ISSN 2072-4292. doi: 10.3390/rs4092753. URL http://dx.doi.org/10.3390/rs4092753.

A. Y. Ng, M. I. Jordan, and Y. Weiss. On spectral clustering: Analysis and an algorithm. *Advances in neural information processing systems*, 2:849–856, 2002. ISSN 1049-5258. doi: 10.1.1.19.8100.

E. Rignot, J. Mouginot, and B. Scheuchl. Ice flow of the antarctic ice sheet. *Science*, 333(6048):1427–1430, 2011. ISSN 0036-8075. doi: 10.1126/science.1208336. URL https://science.sciencemag.org/content/333/6048/1427.

N. Santitissadeekorn and E. Bollt. Identifying stochastic basin hopping by partitioning with graph modularity. *Physica D: Nonlinear Phenomena*, 231(2):95–107, 2007.

T. Scambos, J. Bohlander, and B. Raup. Images of antarctic ice shelves. modis antarctic ice shelf image archive. http://nsidc.org/data/iceshelves_images/index_modis.html, 1996. Accessed: 2018-09-17.

J. Shi and J. Malik. Normalized cuts and image segmentation. *IEEE Transactions on Pattern Analysis and Machine Intelligence*, 22(8):888–905, 2000. ISSN 01628828. doi: 10.1109/34.868688.

E. J. Steig, D. P. Schneider, S. D. Rutherford, M. E. Mann, J. C. Comiso, and D. T. Shindell. Warming of the antarctic ice-sheet surface since the 1957 international geophysical year. *Nature*, 457(7228):459, 2009.

NASA. NASA National Snow and Ice Data Center Distributed Active Archive Center. https://nsidc.org/cryosphere/quickfacts/icesheets.html, 2017. Accessed: 2020-04-17.

E. Rignot, J. Mouginot and B. Scheuchl. MEaSUREs InSAR-Based Antarctica Ice Velocity Map, Version 2. [subset:2006-2011]. Boulder, Colorado USA. NASA National Snow and Ice Data Center Distributed Active Archive Center. https://nsidc.org/data/nsidc-0484/versions/2, 2017. Accessed: 2018-09-17.

 # A Figures
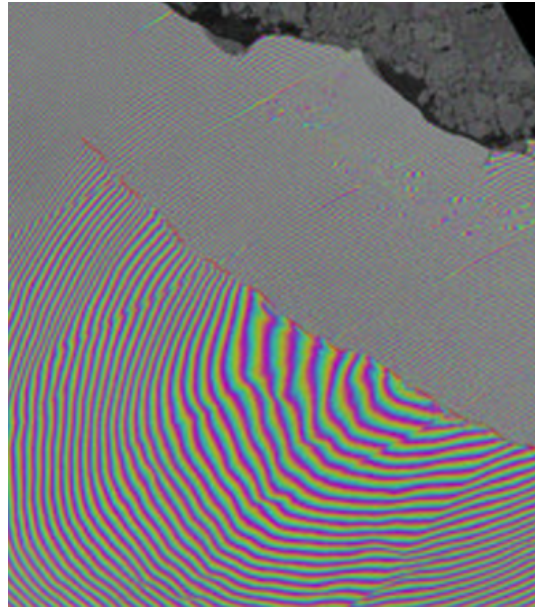
Figure A.1: Interferometry (April 20, 2017). Two Sentinel-1 radar images from 7 and 14 April 2017 were combined to create this interferogram showing the growing crack in Antarctica's Larsen-C ice shelf. Polar scientist Anna Hogg said: "We can measure the iceberg crack propagation much more accurately when using the precise surface deformation information from an interferogram like this, rather than the amplitude (or black and white image) alone where the crack may not always be visible." Source Agency (2017).
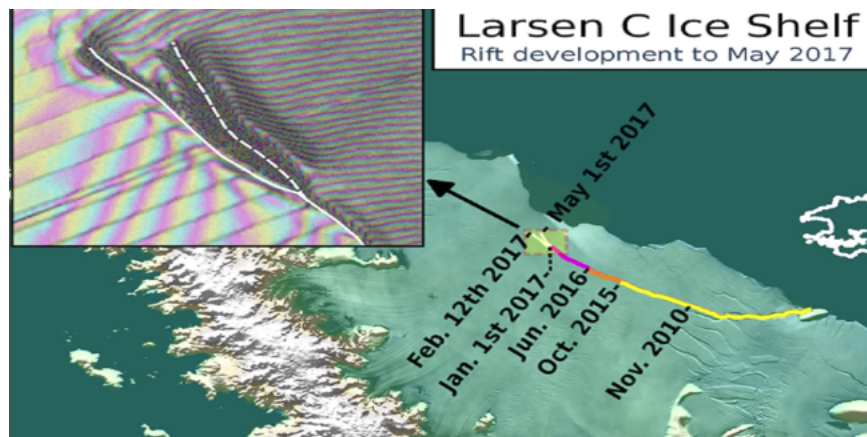
Figure A.2: Lrasen C crack development (new branch) as of May 1, 2017. Labels highlight significant jumps. Tip positions are derived from Landsat (USGS) and Sentinel-1 InSAR (ESA) data. Background image blends BEDMAP2 Elevation (BAS) with MODIS MOA2009 Image mosaic (NSIDC). Other data from SCAR ADD and OSM. Credit: MIDAS project, A. Luckman, Swansea University.

B   More Numerical Results
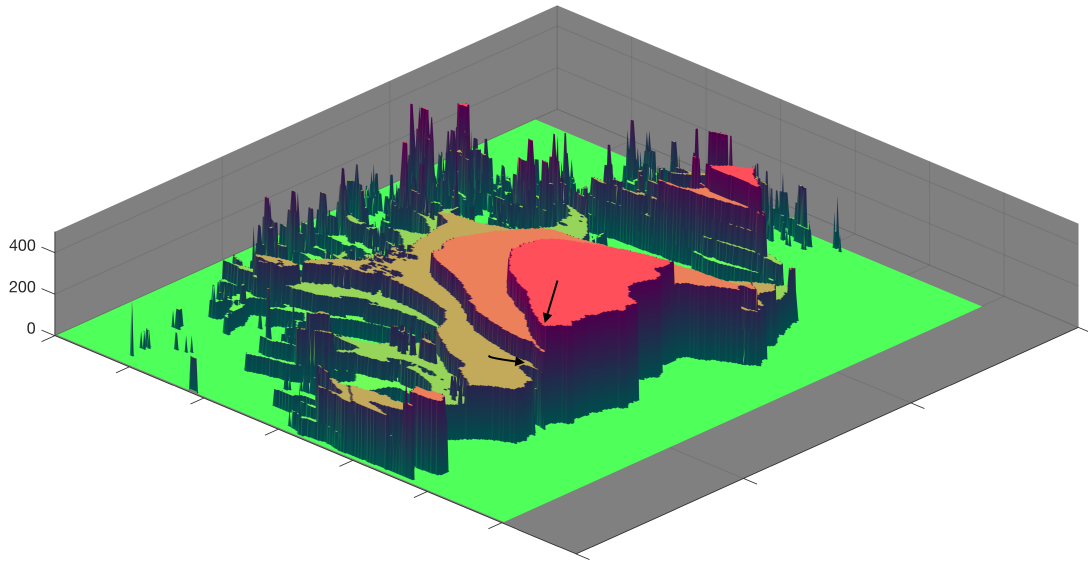
Figure B.1: Directed affinity partitions with the mean velocity (speed) of the partition assigned for each label entries. The spatial distance between the arrows tips is less than two miles, while the difference in the speed is more than 200 m/year.
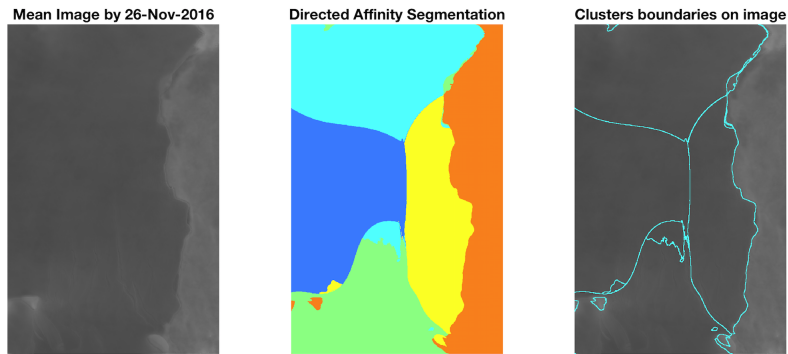
Figure B.2: The mean image and the directed affinity partitioning as of November 2016. The results shows similar structure to the crack branching that occurred on May 2017 and shown in Fig. A.2, and similar structure the final iceberge that calved from Larsen C on July 2017. Raw images source Scambos et al. (1996).
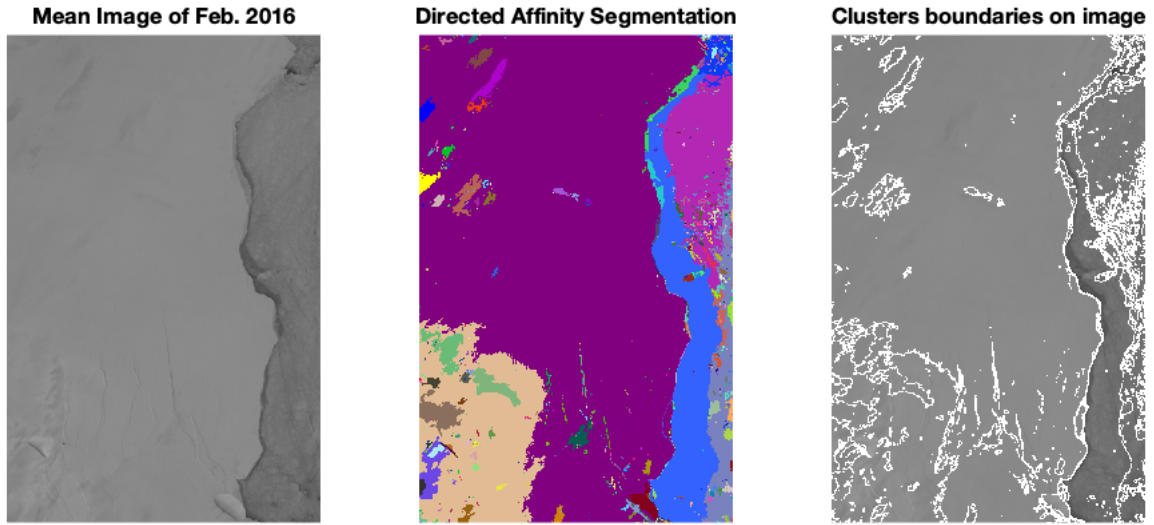
Figure B.3: The mean image and the directed affinity partitioning as of February 2016. Raw images source Scambos et al. (1996).
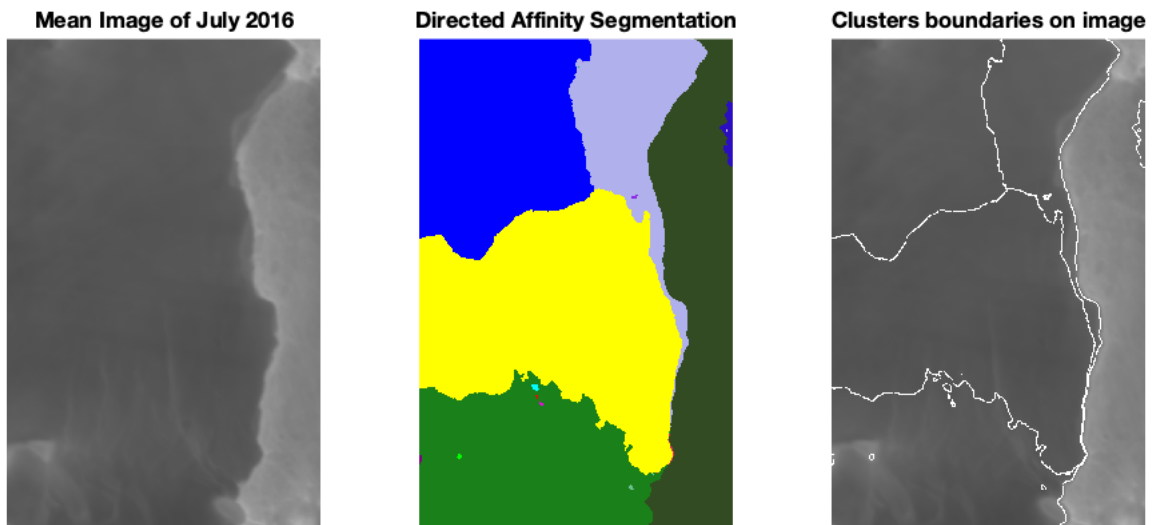
Figure B.4: The mean image and the directed affinity partitioning as of July 2016. Raw images source Scambos et al. (1996).
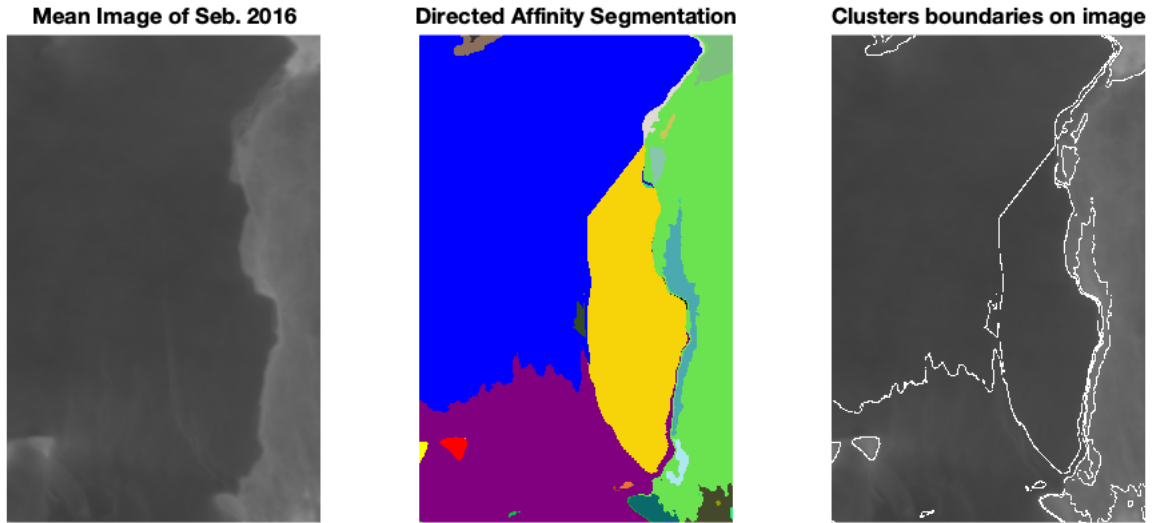
Figure B.5: The mean image and the directed affinity partitioning as of September 2016. Raw images source Scambos et al. (1996).
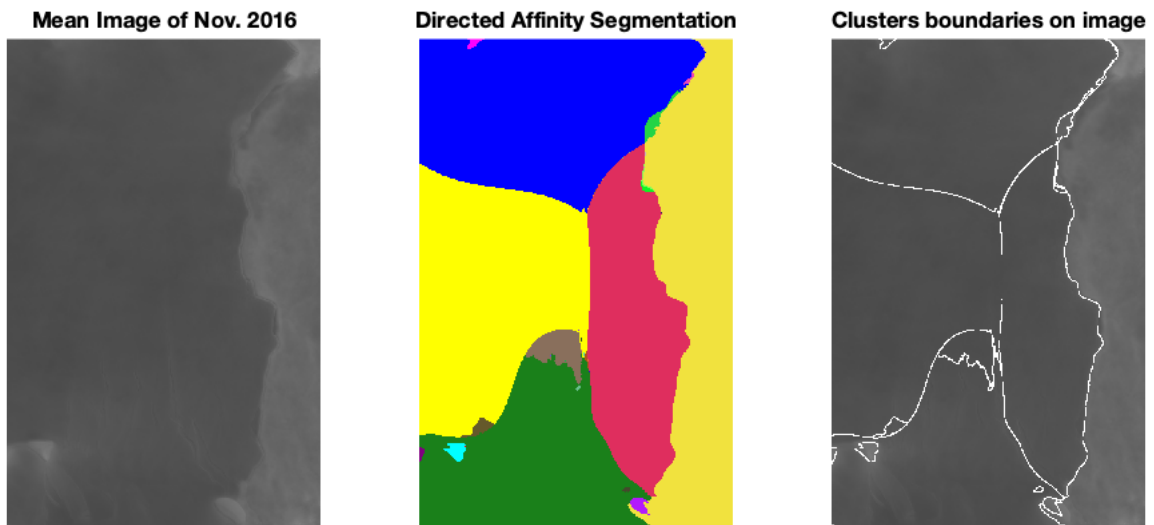
Figure B.6: The mean image and the directed affinity partitioning as of November 2016. Raw images source Scambos et al. (1996).
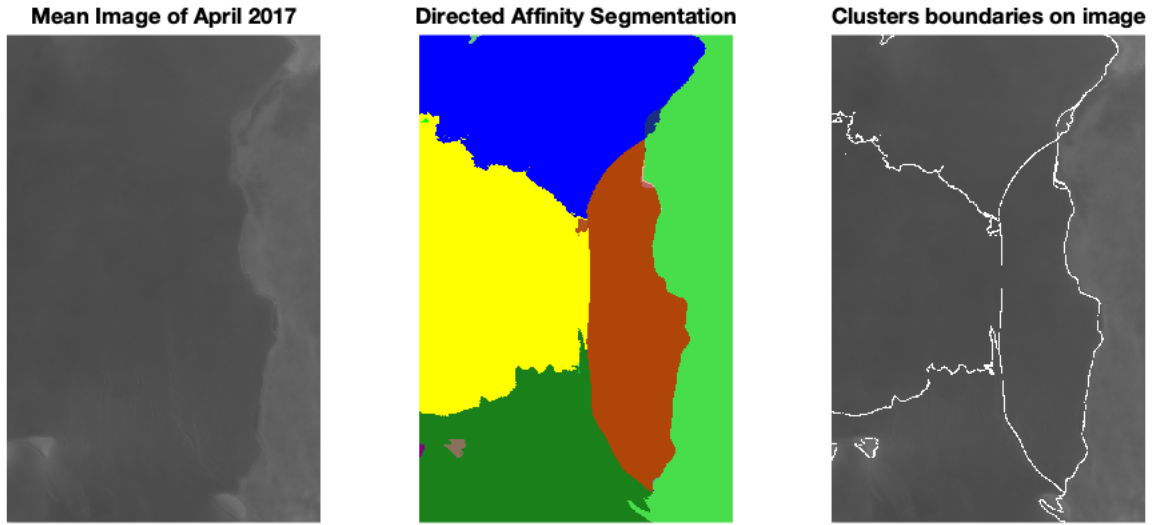
Figure B.7: The mean image and the directed affinity partitioning as of April 2017. Raw images source Scambos et al. (1996).